High Power Laser Science and Engineering, (2023), Vol. 11, e85, 14 pages.
doi:10.1017/hpl.2023.50

HIGH POWER LASER SCIENCE AND ENGINEERING

RESEARCH ARTICLE

Measurements of plasma density profile evolutions with a channel-guided laser

Tong Yang[1,2], Zhen Guo[1,2], Yang Yan[1,2], Minjian Wu[1,2], Yadong Xia[1,2], Qiangyou He[1,2], Hao Cheng[1,2], Yuze Li[1,2], Yanlv Fang[1,2], Yanying Zhao[1,2,3], Xueqing Yan[1,2,3], and Chen Lin[1,2,3]

[1] *State Key Laboratory of Nuclear Physics and Technology, and Key Laboratory of HEDP of the Ministry of Education, CAPT, Peking University, Beijing, China*

[2] *Beijing Laser Acceleration Innovation Center, Beijing, China*

[3] *Institute of Guangdong Laser Plasma Technology, Guangzhou, China*

(Received 5 January 2023; revised 18 May 2023; accepted 7 June 2023)

Abstract

The discharged capillary plasma channel has been extensively studied as a high-gradient particle acceleration and transmission medium. A novel measurement method of plasma channel density profiles has been employed, where the role of plasma channels guiding the advantages of lasers has shown strong appeal. Here, we have studied the high-order transverse plasma density profile distribution using a channel-guided laser, and made detailed measurements of its evolution under various parameters. The paraxial wave equation in a plasma channel with high-order density profile components is analyzed, and the approximate propagation process based on the Gaussian profile laser is obtained on this basis, which agrees well with the simulation under phase conditions. In the experiments, by measuring the integrated transverse laser intensities at the outlet of the channels, the radial quartic density profiles of the plasma channels have been obtained. By precisely synchronizing the detection laser pulses and the plasma channels at various moments, the reconstructed density profile shows an evolution from the radial quartic profile to the quasi-parabolic profile, and the high-order component is indicated as an exponential decline tendency over time. Factors affecting the evolution rate were investigated by varying the incentive source and capillary parameters. It can be found that the discharge voltages and currents are positive factors quickening the evolution, while the electron-ion heating, capillary radii and pressures are negative ones. One plausible explanation is that quartic profile contributions may be linked to plasma heating. This work helps one to understand the mechanisms of the formation, the evolutions of the guiding channel electron-density profiles and their dependences on the external controllable parameters. It provides support and reflection for physical research on discharged capillary plasma and optimizing plasma channels in various applications.

Keywords: channel-guided laser; discharge capillary; plasma density profile

1. Introduction

Laser–plasma accelerators (LPAs)[1,2] can produce electric acceleration fields of the order of tens to hundreds of GV/m[3,4], making them attractive as compact particle accelerators. This mechanism makes it is possible to reduce the distance required to generate GeV-level electron beams from kilometers to centimeters[5–8]. Thus, it promises to increase the availability of the important resource, highly relativistic, high-brightness electron beams as an essential tool for fundamental and application research, at significantly reduced size and cost. Over the past decade, milestone experiments have verified the key principles of LPAs and the possibility to generate high-brightness beams, featuring electron bunches of low emittance[9,10], multi-femtosecond length and kiloampere peak current[11–13]. These results show that LPAs are, in principle, capable of generating electron beams with competitive beam quality. In particular, significant progress has been made on LPAs yielding quasi-monoenergetic electron beams[14–16] with the highest energy record in three steps from 1 to 7.8 GeV by an ultra-intense laser pulse guided in multi-cm-long gas-filled capillary discharge waveguides[6–8]. In the preformed

Correspondence to: Chen Lin, State Key Laboratory of Nuclear Physics and Technology, and Key Laboratory of HEDP of the Ministry of Education, CAPT, Peking University, Beijing 100871, China. Email: lc0812@pku.edu.cn

plasma density channels, the propagation distance of a laser pulse can reach tens of times larger than the Rayleigh length. Experimental studies and solutions of an efficient approach to coupling laser pulses with high mode quality to a preformed plasma channel waveguide have made important contributions to advancing the field of LPAs.

For the application, it is highly desirable that the laser pulse should propagate extended distances (many Rayleigh lengths) at high intensity. In the absence of an optical guiding mechanism, the propagation distance is limited to approximately a Rayleigh (diffraction) length $Z_R = \pi r_0^2/\lambda$, where λ is the laser wavelength and r_0 is the laser spot size at focus. High intensities require a tight focus and, consequently, a relatively short Rayleigh length. However, the limitation may be breached over distances of several centimeters, utilizing preformed plasma density channels. An approach for creating density channels is to use slow gas-filled capillary discharges[17]. In the device, instead of an auxiliary laser, a current pulse is passed through a capillary with an inner diameter of a few hundred micrometers and scaling length of several or even tens of centimeters, prefilled with gas at a pressure of tens to hundreds of millibars. The current pulse has a peak of a few hundred amperes and a duration of the order of hundreds of nanoseconds. Capillary discharges have been used to create straight or curved plasma channels, in which laser pulses have been guided over many Rayleigh lengths[17–24]. Gas-filled capillary discharge waveguides offer a number of advantages in guiding intense laser pulses, such as low transmission and coupling losses. This is a mainstream and popular stabilization method with a parabolic density profile, which allows the propagation of Gaussian laser pulses with a constant matched spot size radius[25,26].

Furthermore, advanced concepts with capillary discharges have demonstrated novel injection techniques[27–31], the generation of plasma-driven X-ray pulses[32,33], synchrotron radiations[34] and high harmonics[35], cascade acceleration schemes[36–38], energy dechirpers[39–41] and the transport of LPA electron[35,42–50] and proton beams[51,52] as novel active plasma lenses (APLs). In particular, APLs have a focus gradient of up to several kT/m. Combined with the laser–plasma acceleration, it is hoped to realize the miniaturization of particle accelerators. However, the quality of beam transports would be degraded in APLs with non-uniform current densities, which are closely related to the plasma electron-density profiles. In addition, for all the applications above, gas-filled capillaries offer the ability to continuously tune the plasma pressure and long device lifetimes. Furthermore, in the case of gas-filled capillaries, the plasma channel may be fully ionized, which minimizes spectral or temporal distortion, which is helpful for sensitivity of measurement. For both channel-guided lasers and beams, the measurements of plasma channel density profiles are important evidence.

In general, refractive guiding of optical pulses can occur when the transverse (radial) profile of the index of refraction η is peaked along the propagation axis. A plasma column or channel with a transverse electron-density minimum on the axis has $\partial\eta/\partial r < 0$ and thus produces the desired refractive index profile for guiding, where r is the radial component. Specifically, a plasma channel with a radially parabolic density profile of the form $n(r) = n_0 + \Delta n r^2/r_0^2$ can guide a laser pulse of spot size r_0 provided the channel depth satisfies $\Delta n = \Delta n_c$, where n_0 is the density in axis, $\Delta n_c = 1/\pi r_e r_0^2$ is the critical channel depth and $r_e = e^2/\left(4\pi\varepsilon_0 m_e c^2\right) = 2.8 \times 10^{-15}$ m is the classical electron radius[53,54]. It has been shown that the presence of the plasma channel leads to betatron oscillations of the laser spot, which allows the laser to be confined close to the axis of channels. There is a great deal of research work[55–61] devoted to analyzing the optical guiding of laser pulses in plasma channels, for example, solving the paraxial wave equation with nonlinear source terms using the well-known source-dependent expansion (SDE) method[62,63]. In particular, previous research built the basis of quasi-matched spots for higher-order density profiles beyond parabolic ones[64], the laser propagation with a mismatched spot was analyzed[65] and matched Laguerre–Gaussian modes in high-order plasma channels were proved[66].

In the gas-filled capillary discharge, the plasma channel is formed by the temperature profile during discharge, which is higher in the center as a result of the ohmic heating effect of plasma and drops radially because the heating is balanced by heat conduction to the capillary wall[67,68]. Measurements of the transverse electron-density profile in a hydrogen-filled device have shown that a quasi-parabolic plasma channel is indeed formed[69]. In the outer edge of a plasma channel, the density profile described by a parabola alone is not sufficient, because the quasi-thermal equilibrium conditions may be violated due to large temperature gradients and violent particle collisions. It is worth paying attention to the impact of experimental non-ideal parabolic density distributions on applications, since the density dominates the plasma response time, self-injection threshold, accelerating field strength, electron beam dephasing length[3], beam-driven wakefield effects[44], spatial distribution of the discharge current density, phase space development of charged particles during transport[43,44] and radiation generating phase matching conditions[70].

Different application scenarios need to adapt to the density distribution under different time windows. For instance, the time window of the plasma channel as the best matching guide waveguide is only less than tens of nanoseconds. Knowledge of the plasma density profile evolution is of critical importance to optimizing the performance of the channel. Current techniques for measuring the density channel profiles in a gas-filled capillary discharge waveguide are inadequate. Longitudinal interferometry experiments

https://doi.org/10.1017/hpl.2023.50 Published online by Cambridge University Press

with a Mach–Zehnder interferometer require the capillary length to be less than a few millimeters, resulting in measurement error associated with end effects[69,71,72]. Transverse interferometry measurements require capillaries that are square, necessitating strong assumptions about the symmetry of the profile[73–78] and flat optical side windows to provide the optical path. The well-known spectroscopic method using the Stark broadening effect loses the ability to spatially resolve[79–81]. An alternative way to detect the plasma density, based on the shock waves produced by gas discharge in a capillary[82], yields only integrated axial distribution information and must be calibrated by other methods. Spot size measurements at the output of the capillary have also been used to deduce channel depth[83,84], but this technique requires several plasma channels with different lengths while keeping other parameters consistent. Another method employs the observation of Raman shifts in the guided laser spectrum, but this requires high laser power[85,86]. The group velocity delay[87] of a laser pulse and the common-path two-color interferometer[88,89] can only be correlated with the on-axis plasma density. Extensive research has been carried out to gather more details on the shape of the channel and accurate diagnostics of the paraxial plasma channel depth by the method of measuring laser centroid oscillations[90], and the quartic density distribution of plasma channels is first introduced into measurement research[90,91]. On the other hand, in order to assist the development of this channel, important simulations[67,68,92] of the plasma dynamics of a hydrogen-filled capillary discharge have been studied to understand the mechanisms by which the guiding electron-density profile is formed and how its properties depend on the external, controllable parameters.

In this paper, we report the measurement of the temporal evolution of the electron-density profile, in particular, including marginal higher-order distributions in a gas-filled discharge capillary by distinguishing channel-guided laser mode quality. Adopting a collimated laser eliminates the influence of the divergence angle of the probe laser to ensure accuracy. The intensity was kept low ($< 10^{14}$ W/cm^2) in these experiments so that nonlinear effects such as self-focusing, wake formation and hosing could be neglected and the plasma properties were measured in a straightforward way. This method relies on the fact that the radial density profiles in gas-filled capillary discharge waveguides mainly depend on three parameters, namely the diameter of the capillary, the discharge current profile and the filling gas pressure, in the absence of the longitudinal flow. We shall present the method from three aspects, including the theory in Section 2, simulations in Section 3 and experiments in Sections 4 and 5. The work is aimed to contribute to the in-depth study of the evolution mechanism and properties of plasma channels and to implement optimizations in a variety of applications.

2. Heuristic theory of channel-guided propagation

In this paper, the mathematical model for describing laser pulse evolution is based on the wave equation:

$$\left(\nabla^2 - \frac{1}{c^2}\frac{\partial^2}{\partial t^2}\right)E = k^2\left(1-\eta_{\rm r}^2\right)\widehat{E}, \tag{1}$$

where $E = \mathrm{Re}\left[\widehat{E}e^{ik(z-ct)}\right]$ is the transverse electric field of the laser, $\widehat{E}(r,z,t)$ is the slowly varying amplitude envelope, $\omega = ck = 2\pi/\lambda$ is the laser frequency, k is the laser wave number, λ is the laser wavelength, c is the speed of light in a vacuum, t is a time independent variable, $\eta_{\rm r}$ is the index of refraction of the medium and $\left|1-\eta_{\rm r}^2\right| \ll 1$ is assumed. Here, $\eta_{\rm r}$ is generally a nonlinear function of the medium density profile:

$$\eta_{\rm r} = 1 - \frac{k_{\rm p}^2(r)}{k^2}, \tag{2}$$

where $k_{\rm p}$ is the plasma wave number. In the following, it will be assumed that $\eta_{\rm r}$ is real, that is, dissipative effects such as collisions and absorption will be neglected. The following analysis is carried out under the axisymmetric cylindrical coordinate system, with z being the axial propagation direction and r the radial component:

$$\nabla_\perp^2 = \nabla^2 - \frac{\partial^2}{\partial z^2} \simeq \frac{1}{r}\frac{\partial}{\partial r}\left(r\frac{\partial}{\partial r}\right), \tag{3}$$

where $\partial^2/\partial z^2$ is typically small, which will be neglected.

The propagation of an ultrashort laser pulse in a preformed plasma channel will be considered. Propagation is considered in the limits of low power $P/P_{\rm c} \ll 1$ and low intensity $a_0^2 \ll 1$, such that nonlinear effects (e.g., relativistic self-focusing) can be neglected and the density channel can be assumed to be unaffected by the laser pulse, where P is the laser power, $P_{\rm c}$ is the critical power for relativistic self-focusing and a_0 is the laser relativistic intensity. The starting point for describing laser pulse evolution in plasma is the linear paraxial wave equation[26] for the transverse component of the laser field, which can be written in the following form:

$$\left(\nabla_\perp^2 + 2ik\frac{\partial}{\partial z}\right)\widehat{E} = k_{\rm p}^2(r)E, \tag{4}$$

where $k_{\rm p}^2(r) = k_{\rm p0}^2 n(r)/n_0$, $k_{\rm p0} = \omega_{\rm p0}/c$ is the plasma wave number, $\omega_{\rm p0} = \sqrt{n_0 e^2/(\varepsilon_0 m_{\rm e})}$ is the plasma frequency, n_0 is the electron plasma density on the central axis ($r = 0$), e is the elementary charge, ε_0 is the vacuum permittivity, $m_{\rm e}$ is the electron mass in an international system of units and $n(r)$ is the radial distribution of the plasma channel density that will be introduced below.

https://doi.org/10.1017/hpl.2023.50 Published online by Cambridge University Press

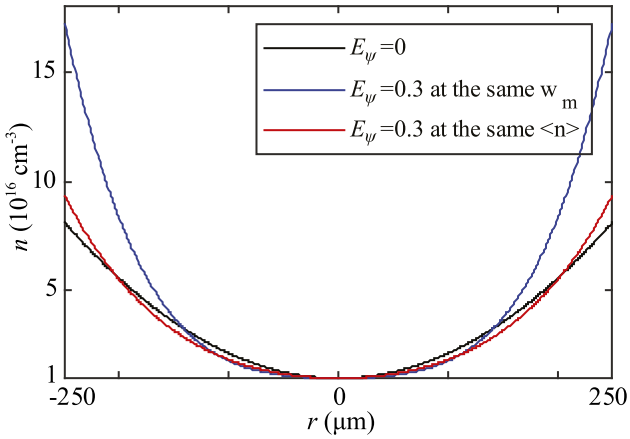

Figure 1. Calculated plasma electron-density profiles $n(r)$ as a function of radial position r with axis density $n_0 = 1 \times 10^{16}$ cm^{-3} and matched spot size $w_m = 100$ μm for a parabolic channel (black line) compared with a channel with an r^4 component with $E_\Psi = 0.3$ at the same w_m (blue line) and a channel at the same $\langle n \rangle$ (red line), respectively.

To analyze the behavior of the pulse radius, consider the local normalized-intensity-weighted mean-squared radius $\langle r^2 \rangle$ defined by the following:

$$\langle r^2 \rangle = \frac{\int_0^\infty r^3 |\widehat{E}|^2 \mathrm{d}r}{\int_0^\infty r |\widehat{E}|^2 \mathrm{d}r}. \tag{5}$$

We say that a laser propagating in a plasma channel satisfies a quasi-matched propagation condition if its second-order $\partial^2 \langle r^2 \rangle / \partial z^2$ remains zero. Plasma channels focus laser pulses due to a radially varying refractive index. Self-steepening and depletion have been neglected to simplify the analysis of the problem. The matched spot size w_m can be obtained from the radial electron-density distribution according to the following[64]:

$$8\pi r_e \int_0^\infty n(r) \left(\frac{2r^2}{w_m^2} - 1 \right) e^{-\frac{2r^2}{w_m^2}} r\mathrm{d}r - 1 = 0. \tag{6}$$

Equation (6) gives the general matched spot size for applicable densities, besides the parabolic density profiles. High-order contributions should be introduced for a complete depiction of density profiles. One model provides an excellent description, as shown in Figure 1, with quartic terms of the outer edge density profile for $|r| > 2w_m$ as follows[91]:

$$n(r) = n_0 + \frac{1 - E_\Psi}{\pi r_e w_m^4} r^2 + \frac{E_\Psi}{2\pi r_e w_m^6} r^4, \tag{7}$$

where E_Ψ is a scaling factor for the relative contributions of the quadratic distribution (r^2 term) and the quartic distribution (r^4 term). r_{ch} is the maximum radius of the outer edge of the channel. Considering a specific plasma evolution over time, the average density $\langle n \rangle = \int_0^{r_{ch}} n(t) r\mathrm{d}r / r_{ch}^2$ is approximately conserved, which will be discussed in the Section 5. The channel can guide multiple matched laser sizes at various moments with various E_ψ, as the black and red lines shown in Figure 1. When it comes to a specific matched spot, multiple matched channels can be produced with various E_ψ and $\langle n \rangle$, as the black and blue lines show in Figure 1. In the description of channel-guided laser physics, the parameters E_ψ, w_m and $\langle n \rangle$ are closely related. Equation (7) can be rewritten into an equivalent form:

$$n(r) = n_0 + \Delta n_{r2} \frac{r^2}{r_{ch}^2} + \Delta n_{r4} \frac{r^4}{r_{ch}^4}. \tag{8}$$

For $E_\Psi < 1$ and $r^2 \ll r_{ch}^2$, a rough approximation can be taken:

$$n(r) \simeq n_0 + \Delta n_{ch} \frac{r^2}{r_{ch}^2} = n_0 + \Delta n_{r2} \left(1 + \frac{\delta \Delta n_{r2}}{\Delta n_{r2}} \right) \frac{r^2}{r_{ch}^2}, \tag{9}$$

where $\delta \Delta n_{r2} = \Delta n_{r4} r^2 / r_{ch}^2 \ll \Delta n_{r2}$.

Approximate forms for the envelope equations describing laser pulse evolution, that is, a solution to the paraxial wave equation (Equation (4)) can be found by the method of the heuristic theory, considering a Gaussian model laser beam with the following form:

$$E = E_s e^{i\theta - (1 - i\varphi_G) \frac{r^2}{w^2}}, \tag{10}$$

where E_s, φ_G, w, θ represent the amplitude, curvature, spot size and phase shift, respectively. Analysis of the paraxial wave equation (Equation (4)) with an index of refraction of an ideal radially parabolic density profile form indicates that the spot size w evolves according to heuristic theory[26]:

$$\frac{\partial^2 w}{\partial z^2} = \frac{4}{kw^2} \left(1 - \frac{w^4}{w_m^4} \right), \tag{11}$$

where the matched beam spot size w_m is given by the following:

$$w_m^4 = \frac{r_{ch}^2}{\pi r_e \Delta n_{ch}}. \tag{12}$$

Note that the high-order density profile component contributes to a mismatched spot as mathematical equivalence:

$$w_m = w_{mM} \left(1 - \frac{1}{4} \frac{\delta \Delta n_{r2}}{\Delta n_{r2}} \right) = w_{mM} + \delta w_m, \tag{13}$$

where $w_{mM} = \sqrt[4]{r_{ch}^2 / (\pi r_e \Delta n_{r2})}$ is the matched spot size of the paraxial density profile. The laser evolution from the paraxial wave equation (Equation (4)), with the initial

https://doi.org/10.1017/hpl.2023.50 Published online by Cambridge University Press

(at $z = 0$) conditions $\varphi_G = 0, \theta = 0, \partial w/\partial z = 0$, is given by the following[65]:

$$E = E_0 \left[1 - \frac{\delta w_m}{w_m}\left(1 - \frac{2r^2}{w_m^2}\right) e^{-ik_{os}z}\right] e^{-\frac{r^2}{w_m^2}}. \tag{14}$$

We can get the radial intensity profile evolution as follows:

$$\begin{aligned} I &= EE^* \\ &= E_0^2 \left\{1 + [\Psi\chi(1-\chi)]^2 - 2\Psi\chi(1-\chi)\cos k_{os}z\right\} e^{-\chi}, \end{aligned} \tag{15}$$

where $k_{os} = 4/\left(kw_m^2\right)$ is the betatron wave number and $\chi = 2r^2/w_m^2$. One coefficient can be defined as

$$\Psi = \frac{1}{8}\frac{\Delta n_{r4}}{\Delta n_{r2}}\sqrt[4]{\pi r_e \Delta n_{r2} r_{ch}^2} \tag{16}$$

to denote the rate of contributions of the r^4 term to that of the r^2 term.

The above proof illustrates the impact of the r^4 term of the electron density on laser intensity distribution in accordance with Equation (15), which is obviously different from the Gaussian model within ideal parabolic density profiles. The employed centroid displacement technique[90] can provide parabolic plasma channel shape information, that is, Δn_{r2}, intuitively. However, without an explicit expression, the measurement of Δn_{r4} generally relies on an iterative agreement between the experimental data and the simulation process. In addition, the intensity distribution measurement as a novel method can get the off-axial density Δn_{r4} at the channel outlet via fitting Equation (15) for a fixed z.

3. Simulation of laser propagation in plasma channels

Actually, it is important to specify the laser mode injected into the plasma channel. In our experiments, the collimated laser used with a particularly large Z_R can be approximated as a plane wave due to its spot size being significantly larger than the radius of the plasma channel. However, the diffraction shaping effect on the pulse wavefront by the electrode hole and capillary wall from the electrode surface to the front end of the plasma channel is usually disregarded, because of the gas inlet position[69]. We implemented a cylindrical 2D-vector integral transform[93] calculation in cylindrical coordinates to approximately explain the infinite diffraction propagation by an ideal scattering boundary (corresponding to an electrode and the capillary wall), as shown in Figure 2(a), where the data on the negative side of the radial axis are obtained by mirroring. The method is efficient in dealing with diffraction but requires extremely high spatial resolution. Within limited computing resources, we set an initial plane wave electric field with a wavelength $\lambda = 1$ μm and a spatial step of 0.1λ in a

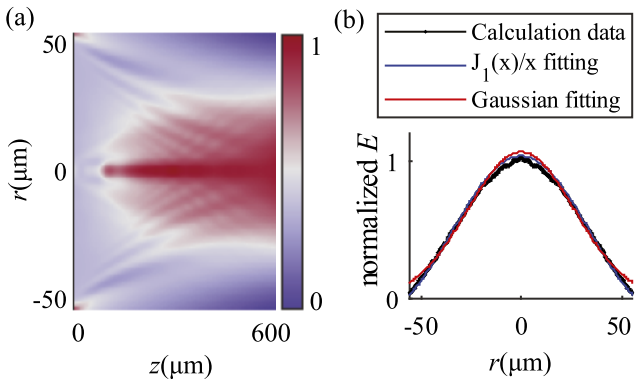

Figure 2. (a) The cylindrical 2D-vector integral transform calculation result of an input plane wave electric field E with wavelength $\lambda = 1$ μm diffraction propagation by an ideal scattering boundary in a 50 μm × 600 μm $(r \times z)$ domain, where the data on the negative side of the radial axis are obtained by mirroring. (b) The normalized transverse E profile at $z = 500$ μm from calculation data (black line) and fitting the profile with the theoretical function $J_1(x)/x$ (blue line) and the approximate Gaussian function (red line) for the channel-guided laser requirement.

50 μm × 600 μm $(r \times z)$ calculation domain. The result of the calculation offers proof of the following, for the propagation of a laser in a capillary with $r_{ch} \gg \lambda$, at only a short distance z that satisfies the Fresnel condition[94]:

$$\frac{z}{2r_{ch}} \geq \sqrt[3]{\frac{2r_{ch}}{\lambda}}. \tag{17}$$

The wavefront can be represented approximately as a Gaussian mode:

$$E = E_0 \frac{2J_1(x)}{x} \simeq E_0 e^{-\frac{r^2}{w^2}}, \tag{18}$$

as shown in Figure 2(b), where $x = x_{10}r/r_{ch}$, J_1 is the first-order Bessel function and x_{10} is the first zero point of $J_1(x)$. In a vacuum, the edge density of a discharge capillary plasma channel drops steeply[79], and the refractive index change of the gas outside the electrode is over two orders of magnitude smaller than that of the plasma[95]. The model could be regarded as input consistent with the quasi-Gaussian mode in Equation (16) at $z = 0$.

In order to check the applicability of the aforementioned heuristic theory introduced, we have performed cylindrical particle-in-cell (PIC) simulations by the Smilei[64] code. The simulated transport domain is 500 μm × 3 cm (corresponding channel radius 250 μm and length 3 cm) in the y–z plane. The simulations consider a plasma channel with a density distribution via the y-direction described in Equation (7) with the ideal matched spot size $w_{mM} = 100$ μm and $E_\psi = 0.3$. According to the theory above, it can be calculated that the channel density depth $\Delta n_{r2} = 7.08 \times 10^{16}$ cm^{-3}, quartic density contribution $\Delta n_{r4} = 1.13 \times 10^{17}$ cm^{-3} and coefficient $\Psi = 0.5002$. Initially, at $t = 0$, a parallel laser

https://doi.org/10.1017/hpl.2023.50 Published online by Cambridge University Press

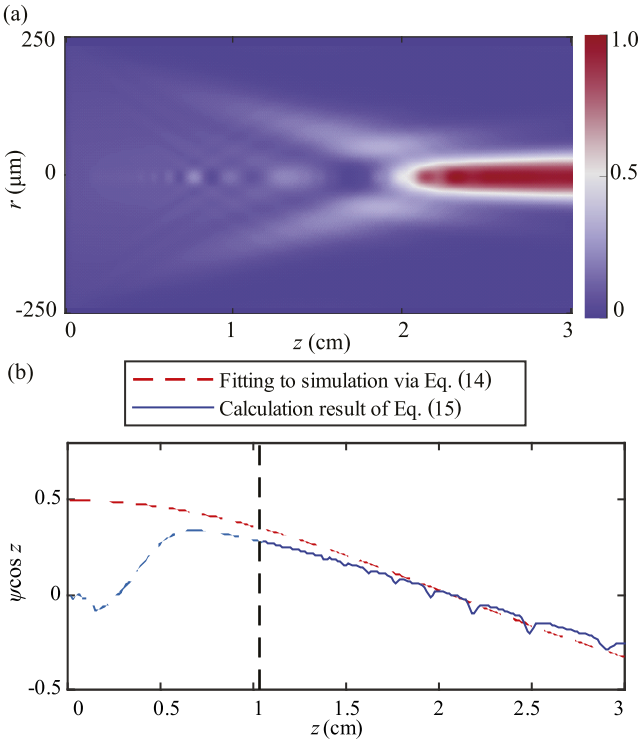

Figure 3. (a) The cylindrical PIC simulation result of a laser with wavelength $\lambda = 1$ μm propagating in plasma with ideal matched spot size $w_{\mathrm{mM}} = 100$ μm and $E_\psi = 0.3$, where the data on the negative side of the radial axis are obtained by mirroring. The simulation domain corresponds to plasma channel radius $r = 500$ μm and length $L = 3$ cm. (b) The coupling parameter $\Psi \cos k_{\mathrm{os}} z$ varying along the z-direction between the fitting to the simulation data via Equation (15) at every z position in the solid blue line and the calculation values of Equation (15) based on the initial set simulation parameters in the broken red line. The two show good consistency after laser propagating at 1.2 cm.

with wavelength $\lambda = 1$ μm is emitted from origin $z = 0$. The betatron wave number $k_{\mathrm{os}} = 0.64$ cm^{-1} can be calculated.

One of the simulation results is given in Figure 3(a). It is obvious that the laser evolves complex models due to introducing a quartic density profile contribution. We fitted the laser intensity profiles along z-direction based on the form of Equation (15). The regularity of the coupling parameter $\Psi \cos k_{\mathrm{os}} z$ from the fitting results is represented by the blue line in Figure 3(b). The numerical result calculated with the above paragraph values along the z-direction is also shown in Figure 3(b) by the broken red line. It can be found that the simulation data well agree with the calculation from its parameters, when satisfying an approximate condition $k_{\mathrm{os}} z \gtrsim \pi/4$. Figure 3(b) shows this condition as a demarcation by a broken black line. The limitation must be pointed out that Equation (15) cannot describe the process from a mismatched spot to a quasi-matched spot. Therefore, the broken light blue line fitting with Equation (15) shown in Figure 3 is unphysical. The condition indicates that there is a limit distance for a parallel laser pulse evolving into the model described by Equation (15), which is related to the focusing ability of the plasma. Meanwhile, it is should be considered that the betatron oscillation damps at a distance of kl_τ/k_{os}[65], which is the upper limit of the capillary length, where l_τ is the laser pulse width. Under such constraints, we adopted discharged plasma in capillaries with channel depth of the order of 10^{17} cm^{-3} and 3-cm length in the experiments.

4. Experimental setup and methods

Figure 4(a) provides a schematic overview of the experimental setup. We used a laser probe pulse to characterize the plasma channel properties. Laser pulses with a wavelength of 798 nm and spot radius of 4 mm were produced by the front end of the new developed terawatt laser system at Peking University as an upgrade part of the Compact LAser Plasma Accelerator (CLAPA)[96]. Collimated laser pulses are exported to the experiment area through a 50:50 beam-splitter downstream of the regenerative amplifier. The pulse energy is less than 0.2 mJ, which is low enough to not modify the channel profile.

The capillary is placed on a motorized hexapod stage that can help to precisely adjust the alignment between a capillary and collimated laser pulses, which will affect the output laser profile. For this paper, the length of all used capillaries is 3 cm and the radii are 150, 250 and 350 μm. The off-axis deviation can be reduced to 33 μrad by judging the concentricity of the continuous diffraction imaging at the exit for 3-cm long capillaries and further to 5 μrad by judging the concentricity of the laser spot in the presence of the plasma channel. The capillary bulk material was either sapphire (Al_2O_3) or a high-temperature laminating (HTL) resin. The HTL resin as a novel 3D-print material that is cheaper can be in a single piece and is easily mechanically machinable. Helium (He) and argon (Ar) are two types of gas that can be filled in the capillary respectively whose pressure can be controlled from 10 to 300 Torr. For the system, the scaling law between the average plasma density and pressure measured from spectroscopy is $\langle n \rangle \left[\mathrm{cm}^{-3}\right] = 2.57 \times 10^{15} \cdot P[\mathrm{Torr}]$. Both capillary ends were open such that gas escapes to the vacuum chamber. During injecting gas, a high voltage of 0–30 kV from the incentive source is applied to the electrodes located at both ends of the capillary, which will lead to gas discharge to generate plasma. A circuit loop is then formed and the plasma is heated to change into a channel by a current pulse with a peak of 100–400 A. Laser pulses can be guided to propagate through the channels at probable time windows. Figure 4(c) shows a photo of plasma channel luminescence during discharge of the gas-filled capillary.

A simple lens imaging system is set for this detection. The distance between the lens with a focal length of 25 cm and the capillary outlet is about 30 cm. The transverse, time-integrated laser pulse profile was imaged with a charge-coupled device (CCD) camera, which has 1600×1200 pixels and a resolution of 0.517 μm/pixel. Figure 4(b) shows

https://doi.org/10.1017/hpl.2023.50 Published online by Cambridge University Press

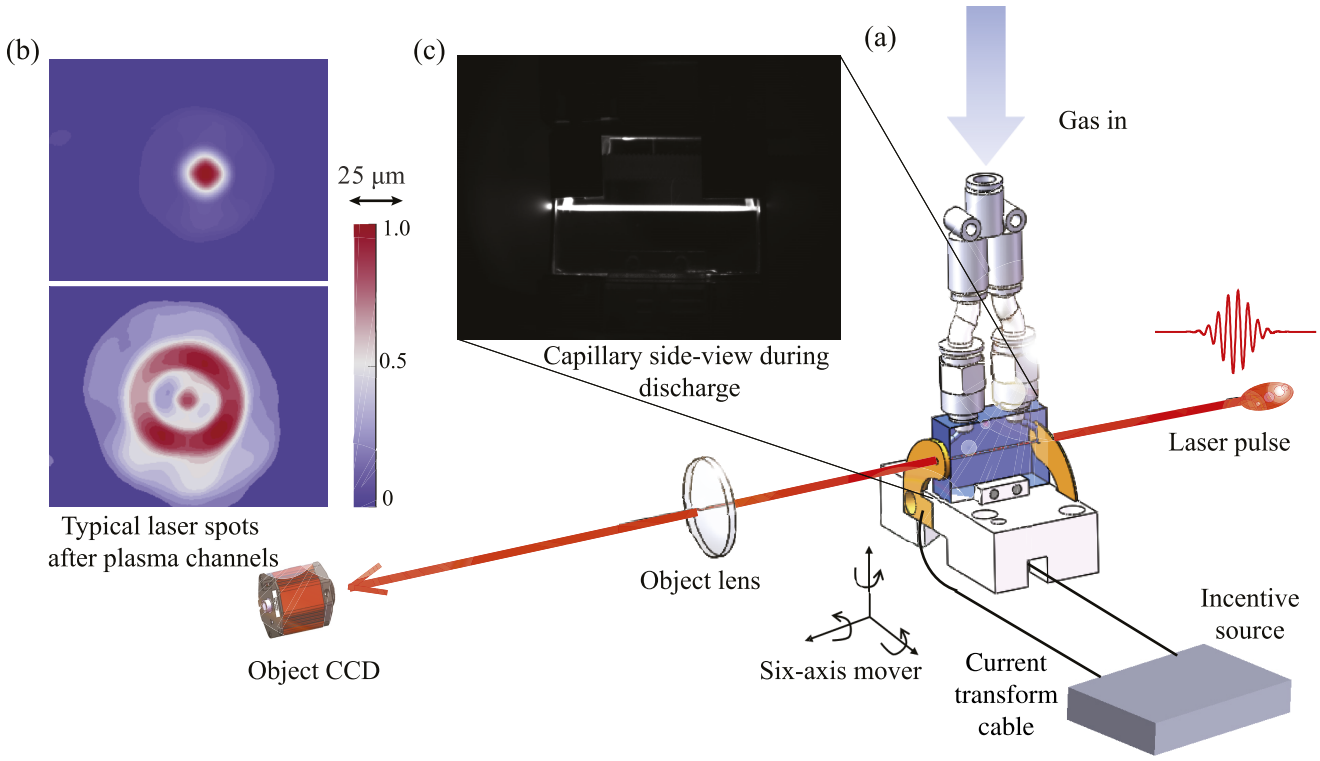

Figure 4. (a) Schematic overview of the experimental setup. Laser pulses propagate from right to left along a capillary as the axis in the z-direction. The capillary is carried by a six-axis mover. Gas is injected from pipes to fill the capillary. Electrodes connected to the incentive source are located at both ends. The imaging system consisting of a single object lens and a CCD is downstream. (b) Typical experimentally measured transverse laser spot intensity distributions at the capillary exit plane during plasma discharge for plasma channels with $\Psi < 0.2$ (the upper subfigure) and $\Psi > 0.5$ (the lower one). (c) Discharge phenomenon of a gas-filled capillary viewed from the side.

examples of measured (single shot, background subtracted) transverse laser pulse intensity distributions at the location of the capillary exit aperture. The upper one represents typical laser spots, which are almost transversely Gaussian, downstream across plasma channel density profiles with $\Psi < 0.2$, where the quartic density contributions can be negligible. The lower one represents those that are no longer fundamental model Gaussian with $\Psi > 0.5$, where the quartic density contributions are obvious in the initial process of plasma channel evolutions, generally.

A DG645 device was used to achieve laser pulses with a repetition rate of 1 kHz propagating through discharged plasma channels at various times, by allocating delay times of the thyratron switch trigger signal referring to the regenerative amplifier trigger signal. The thyratron switch in the incentive source is triggered to close with several ns time jitter. Helmholtz coils are set around current transform cables to get the discharge current time-evolving waveforms and a photodiode was used to get signals when the laser pulses arrived. Both can be measured by an oscilloscope at the same time. The relative time difference between the timing moments of two waveforms is the basis for the time relationship between a laser pulse and a plasma channel.

All the experimental parameter groups are listed in Table 1. As an example, the result of the No. 9 experiment will be analyzed as follows, and is shown in Figure 5. The technique adopted in our example is the simple RLC circuit. The selectable ranges of the resistance (R), inductance (L) and capacitance (C) are 0–500 Ω, 0–18 μH and 0.5–30 nF, respectively. A principle $R^2 \approx 2L/C$ followed makes the current waveform, shown in Figure 5 by the solid red line, approximate to a single sine pulse to suppress electromagnetic impacts from the discharge on the electronic equipment, which can be described as follows:

$$I = I_0 e^{-\alpha t} \sin \omega t, \quad t > 0, \tag{19}$$

where α and ω are the decline and oscillation time scale, respectively. The fitting curve shown in Figure 5 based on Equation (19) of the current waveform can provide the time origin of the discharge. The CCD is synchronously triggered by the DG645 device and is able to acquire the transverse, time-integrated intensity profile of the laser pulses. The quasi-Newton algorithm[97] and the model identification technique[98] can be studied to fit the intensity images with Equation (15). The two rows of subfigures are respectively the experiential profiles (lower ones) and the reconstructed profiles via fitting results (upper ones) in Figure 5, where the intensity is normalized. Notice that the pulse is no longer transversely fundamental Gaussian. The subfigure groups

https://doi.org/10.1017/hpl.2023.50 Published online by Cambridge University Press

Table 1. Parameters for all experimental groups.

Number	Voltage	Gas	Waveform style	Diameter	Pressure	Decline rate ς
1	15 kV	He	Style 3	500 μm	100 Torr	12.06 μs^{-1}
2	20 kV	He	Style 3	500 μm	100 Torr	15.43 μs^{-1}
3	25 kV	He	Style 3	500 μm	100 Torr	16.51 μs^{-1}
4	28 kV	He	Style 3	500 μm	100 Torr	20.96 μs^{-1}
5	15 kV	Ar	Style 3	500 μm	100 Torr	12.92 μs^{-1}
6	20 kV	Ar	Style 3	500 μm	100 Torr	17.85 μs^{-1}
7	25 kV	Ar	Style 3	500 μm	100 Torr	18.61 μs^{-1}
8	28 kV	Ar	Style 3	500 μm	100 Torr	24.00 μs^{-1}
9	20 kV	He	Style 1	500 μm	100 Torr	5.72 μs^{-1}
10	18 kV	He	Style 2	500 μm	100 Torr	9.28 μs^{-1}
11	20 kV	He	Style 1	300 μm	100 Torr	34.47 μs^{-1}
12	20 kV	He	Style 1	700 μm	100 Torr	5.29 μs^{-1}
13	20 kV	He	Style 1	500 μm	80 Torr	20.41 μs^{-1}
14	20 kV	He	Style 1	500 μm	90 Torr	14.52 μs^{-1}

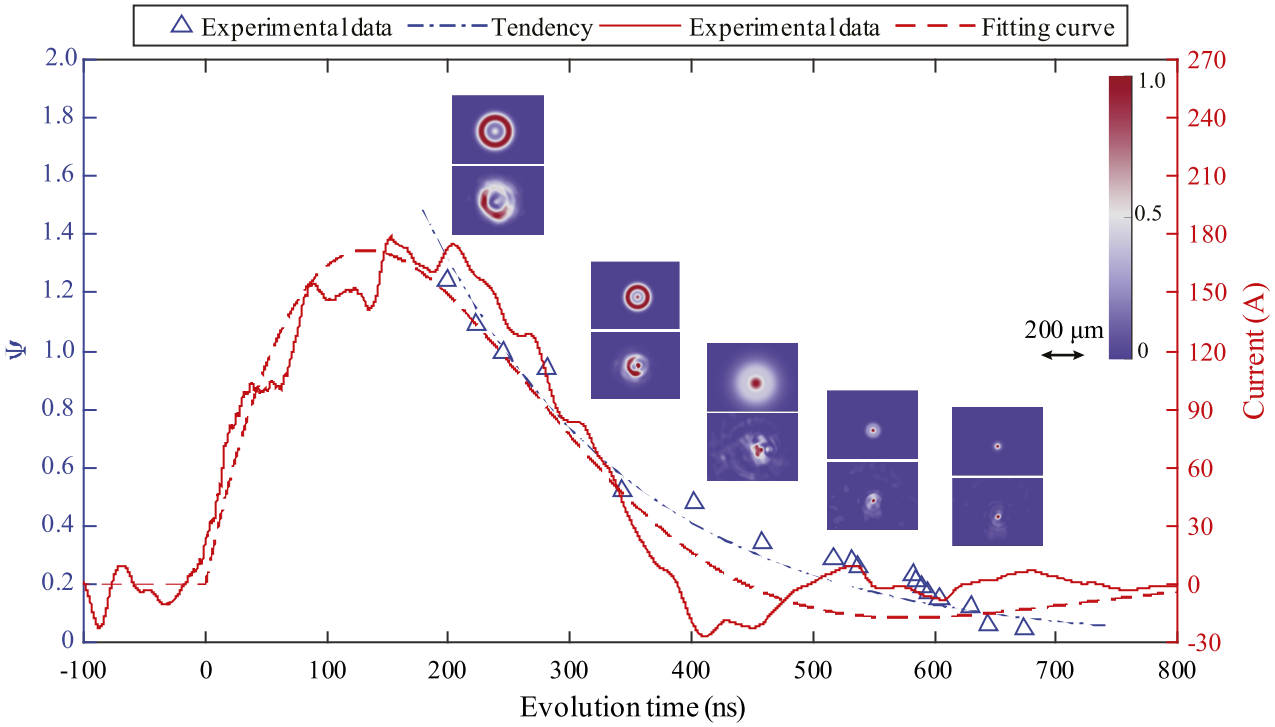

Figure 5. Current waveform measured in the No. 9 experiment shown with a solid red line and fitting results with the waveform based on Equation (19) shown with a broken red line, reconstructed evolution of Ψ from experimental data shown with blue triangle marks and an exponential decline tendency of Ψ evolution shown with a dotted blue line. Both of the red curves above have the *y*-axis on the right in red. Both of the blue curves have the *y*-axis on the left in blue. Subfigure groups made up of a lower one, a measured profile and an upper one, a reconstructed profile via fitting results, in the same column from left to right, correspond to a laser pulse propagating through plasma channels at 245, 343, 458, 537 and 644 ns, respectively. All subfigures are under the unified ruler and color bar placed in the upper right corner inside.

(both in every column) from left to right correspond to a laser pulse propagating through plasma channels at 245, 343, 458, 537 and 644 ns, respectively. The unified ruler and color bar are placed in the upper right corner inside Figure 5. The blue triangle marks are coefficients Ψ defined in Section 2 reconstructed from the fitting results with the experimental measurements. It is almost certain that there is an exponential decline tendency $e^{-\varsigma t}$ of Ψ, which indicates that the r^4 density contribution decreases in the whole current heating process. It is related to the current drop from the peak over time. The coefficient ς can be defined as a time-dependent decline rate to denote the decrease rate of Ψ, that is, the contribution of a quartic density profile. For the case in Figure 5, $\varsigma = 5.72\ s^{-1}$ from the fitted dotted blue line.

5. Experimental results and discussion

In previous work, the impact of discharge voltages and avalanche processes[99] on the development of subsequent plasma channels was rarely considered. Here, we evaluated the influence of the discharge voltages on plasma

https://doi.org/10.1017/hpl.2023.50 Published online by Cambridge University Press

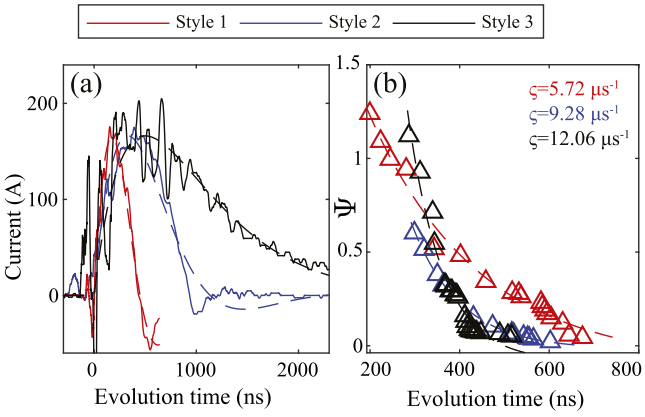

Figure 6. (a) Measured (solid lines) and fitting (broken lines) current waveforms of Style 1 in red, Style 2 in blue and Style 3 in black with $\omega = 6.985$, 2.764 and 0.017 μs^{-1} respectively in the No. 9, No. 10 and No. 1 experiments correspondingly. (b) Reconstructed evolutions of density profile coefficient Ψ shown with triangle marks and exponential decline tendencies shown with broken lines with various styles of waveforms in No. 9 (red), No. 10 (blue) and No. 1 (black) experiments.

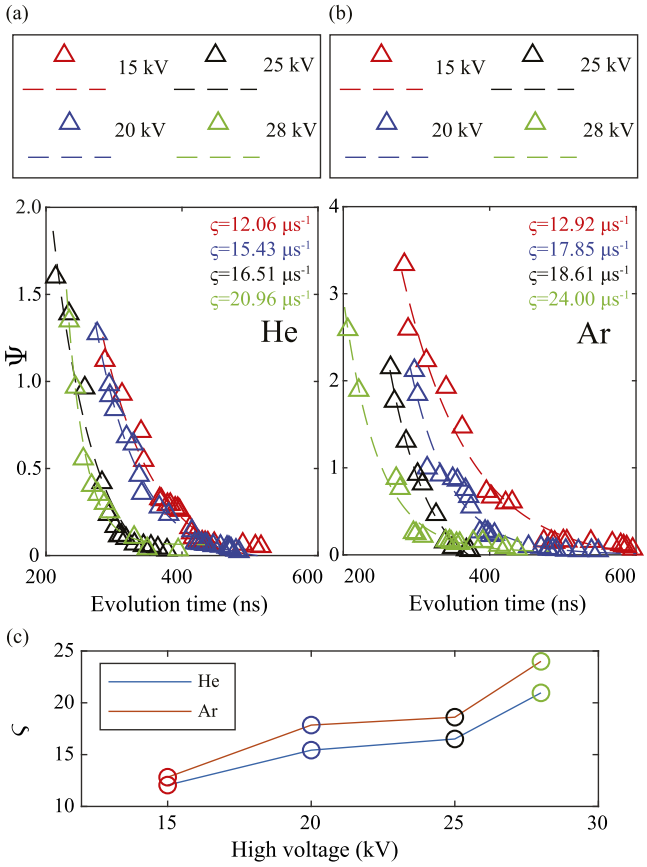

Figure 7. Reconstructed evolutions of density profile coefficient Ψ shown with triangle marks and exponential decline tendencies shown with broken lines (a) with various high voltages $V = 15$, 20, 25 and 28 kV for He plasma in the No. 1 (red), No. 2 (blue), No. 3 (black) and No. 4 (green) experiments, (b) with various high voltages $V = 15$, 20, 25 and 28 kV for Ar plasma in the No. 5 (red), No. 6 (blue), No. 7 (black) and No. 8 (green) experiments. (c) Scaling of the exponential decline rate ς with high voltages for He plasma shown with the light-blue line and Ar plasma shown with the light-red line. The circle marks are in colors corresponding to those in (a) and (b).

density evolution with quartic distributions by three styles of waveforms with different current pulse widths keeping the peak currents the same as much as possible, as shown in Figure 6(a). The three different styles of waveforms are obtained by adjusting circuit parameters R, L and C simultaneously. It is difficult to ensure the same current waveform. Only if the high voltages V of Styles 1–3 are respectively 20, 18 and 15 kV, the peaks are almost equal, that is, those of the No. 9, No. 10 and No. 1 experimental groups. The waveform oscillation time scale ω can be reconstructed as 6.985, 2.764 and 0.017 μs^{-1}, respectively, which is a highly discriminative parameter. However, for such short current pulses, the characteristic parameters of the current transmission loop strongly depend on the current itself. Gas-filled capillaries are small enough loads to neglect. The plasma channel-guided effect starts almost between 200 and 300 ns after the current time origin.

At the rising edge of the current, the gas is rapidly broken down and transformed into almost fully ionized plasma. Discharge voltages positively push the process via more electron emissions[99]. From around the current peak moment, the non-uniform plasma profile is formed and begins to evolve. The evolution process is positively correlated with the current, resulting in the heating effect. In order to evaluate the impact of the breakdown on the evolution, we manipulated the incentive source to generate plasma in a waveform with a higher voltage but a smaller heating current, that is, a steeper falling edge of the current. The decline ς of Ψ still decreases with the current, as shown in Figure 6(b), which infers that the gain from voltages is not enough to offset the reduction in current, and the impact of the breakdown can be negligible compared to that of current heating.

For the same style of waveform with almost the same oscillation scale ω, currents are almost positively linearly related to voltages. In the experiments with the same style waveform, the circuit parameters R, L and C are fixed and adjusting voltages would make the peak currents change. In the following analysis of the influences, it is clear that the effect from currents is dominant compared to that of the voltages.

In order to clarify the influence of the experimental conditions on the profile evolutions, we adopt the control variable method for group comparisons listed in Table 1. Figure 7(a) shows reconstructed profile evolutions with triangle marks and exponential decline tendencies with broken lines with various high voltages $V = 15$, 20, 25 and 28 kV respectively in red, blue, black and green corresponding to the No. 1, No. 2, No. 3 and No. 4 experiments for He plasma. Figure 7(b) shows those in the No. 5, No. 6, No. 7 and No. 8 experiments for Ar plasma. Both Figures 7(a) and 7(b) evidence that ς increases with voltage increasing, essentially that is an increase in the heating effect of the current, which

https://doi.org/10.1017/hpl.2023.50 Published online by Cambridge University Press

is shown in Figure 7(c). Meanwhile, they also evidence that ς of Ar plasma is larger than that of He plasma, as shown in Figure 7(c). It can be interpreted that the discharge of Ar plasma is accompanied by weaker electron-ion heat conduction[45].

Figure 8(a) shows reconstructed profile evolutions with triangle marks and exponential decline tendencies with broken lines with various capillary diameters $d = 300$, 500 and 700 μm, respectively in red, blue and black corresponding to the No. 11, No. 9 and No. 12 experiments, which evidences that ς increases with diameters decreasing, as shown in Figure 8(c). Figure 8(b) shows reconstructed profile evolutions with triangle marks and exponential decline tendencies with broken lines with various capillary pressures $P = 80$, 90 and 100 Torr, respectively in red, blue and black corresponding to the No. 13, No. 14 and No. 9 experiments, which evidences that ς increases with pressures decreasing, as shown in Figure 8(d). The capillary load is small enough that the difference in the parameters of the capillaries themselves hardly affects the circuit characteristics. It is a widely held view that current densities depending on diameters and plasma densities depending on pressures are important factors for local plasma heating. When the current is the same, less plasma will be heated to a higher temperature in less time. Besides, more advanced techniques are needed to address the starting moment of the channel-guided effect experimentally. The problem brings some disturbance to the analysis.

From the experimental results, we can roughly describe the phenomenon of the plasma channel evolution. Previous research work[67,68,92] has described the ohmic heating model of plasmas under quasi-thermal equilibrium conditions. It is the basis on which the $J-T$ model[67] is well suited for parabolic density distributions. We could consider that the parabolic density distribution indicated by the model $n(r)/n_0 = 1 + ar^2/r_{ch}^2$ is approximately valid when $\Psi \to 0$, where a is a main current-related parameter that needs to be measured[68]. A rough evolution hypothesis can be described by the conservation of the number of particles $\partial \langle n \rangle / \partial t = 0$ in the plasma channel. The evolution is from a significant quartic density distribution to a parabolic density distribution holding average constant. However, the approximation is limited as the sub-microsecond timescale is close to the characteristic timescale of acoustic velocity.

So far, the quartic density profile evolution at the outer edge of the channel has not been succinctly described as a brief model. We suspect that this has a great deal to do with heat conduction, nonlocal thermal equilibrium, potential balance and particle collisions and diffusion with the wall material. Probably, it is a reasonable explanation to associate quartic density profile contributions with the plasma presheath of arc discharges[100]. Due to the conservation of particle numbers, the density at the outer edge of channels is positively correlated with the plasma temperature in the central channel region. Obviously, the same goes for the temperature at the edge. Thus, the thickness of the presheath is negatively correlated with temperature. In this way, the profile evolution process is linked to the initial temperature rise of the central plasma. To a certain extent, Ψ and ς would physically express the temperature and temperature rate, respectively. It is possible to introduce why voltages and currents are positive factors to quicken plasma evolutions, and electron-ion heat conduction, radii and pressures are negative. We consider that quickening plasma evolutions is equivalent to increasing the exponential decline tendency coefficient ς of the rate Ψ of the quartic density contribution.

The density profile evolution offers additional ideas for optimizing the plasma channel. For applications of capillaries such as guiding ultra-intense laser pulses and laser–plasma acceleration, ideal parabolic density profiles seem to require sufficient plasma heating but within larger temperature gradients. The laser–plasma relativistic interactions

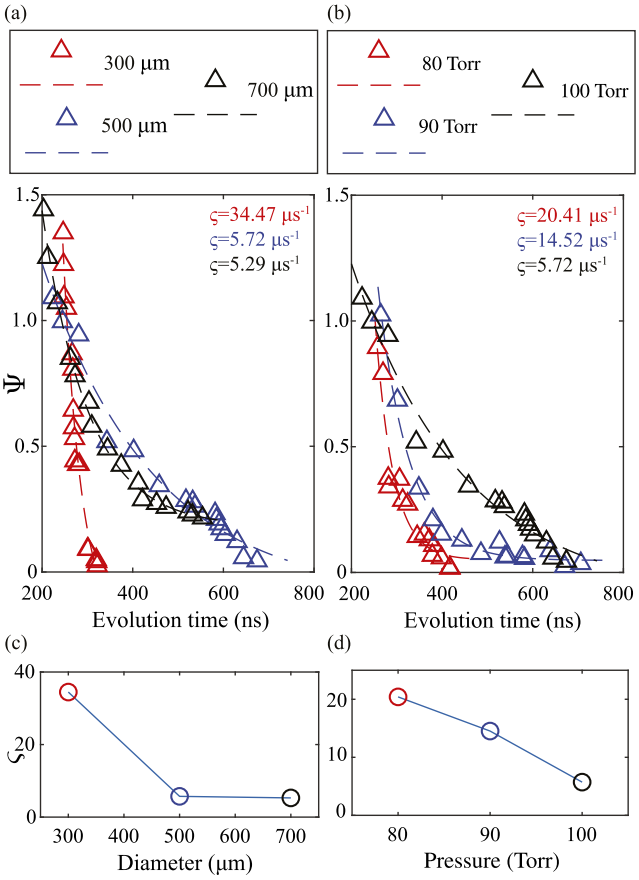

Figure 8. Reconstructed evolutions of the density profile coefficient Ψ shown with triangle marks and exponential decline tendencies shown with broken lines (a) with various capillary diameters $d = 300$, 500 and 700 μm in the No. 11 (red), No. 9 (blue) and No. 12 (black) experiments, and (b) with various pressures $p = 80$, 90 and 100 Torr in the No. 13 (red), No. 14 (blue) and No. 9 (black) experiments. (c) Scaling of the exponential decline rate ς with diameters. The circle marks are in colors corresponding to those in (a). (d) Scaling of the exponential decline rate ς with pressures. The circle marks are in colors corresponding to those in (b).

https://doi.org/10.1017/hpl.2023.50 Published online by Cambridge University Press

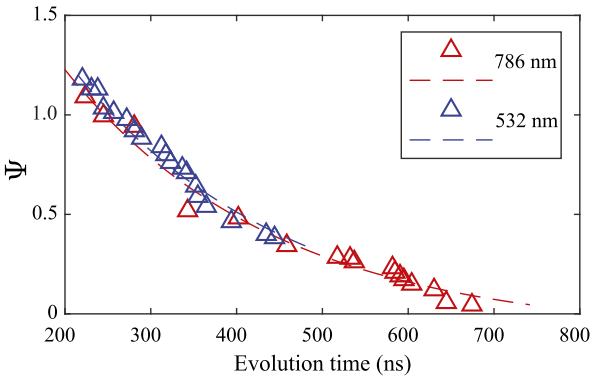

Figure 9. Reconstructed profile evolutions shown with triangle marks and exponential decline tendencies shown with broken lines from measurements with laser wavelength $\lambda = 786$ nm of the front (red) end and $\lambda = 532$ nm of a Q-switched laser (blue), respectively.

considering quartic profile contributions remain unstudied. For charged particle beam transports with plasma channels as APLs, the current density profile is a crucial factor. Plasma with almost entirely parabolic distributions and large temperature gradients is not conducive to maintaining beam emittance. Far from quasi-thermal equilibrium conditions, the impact of quartic profile contributions on the current density profile is unknown. A balance should be found on whether to change circuit parameters or to choose different plasma synchronous moments when searching for the desired currents.

One more experiment was carried out with the same contributions but with laser wavelength $\lambda = 532$ nm in the No. 9 experiment. We deployed a Q-switched laser. Equations (12)–(16) do not exhibit a significant dependence on wavelength. Figure 9 confirms this. The reconstructed profile evolutions measured by the laser pulses from the front end shown with red triangle marks and the Q-switched laser shown with blue ones have a good consistency. The trigger of the latter is subjected to severe electromagnetic shock from the plasma discharges, resulting in a shorter time window for measurements. The slight difference between the two tendencies comes from the sensitivities of different photodiodes, possibly.

6. Conclusions

Inspired by previous research, we study the channel-guided laser propagation in plasma channels with quartic density profiles. For a given plasma distribution, an approximate intensity evolution of the channel-guided laser is concluded. Under the assumption in the presence of the longitudinal flow and axisymmetric distribution, the laser intensity distribution at the outlet of the fixed-length plasma channel corresponds to the density profile information. The evolution process of a plasma density profile would be given by measurements of transverse, time-integrated laser intensity profiles at various times. We define a characteristic coefficient that is appropriate to describe the problem. In particular, the evolution processes of channel plasma density profiles with quartic density profile contributions may be described as an exponential decline tendency of the coefficients over time. The factors influencing the decline rate that characterized the profile evolution speed, including but not limited to circuit parameters, capillary diameters, types of gases injected and pressures, were studied experimentally. It can be found that voltages and currents are positive factors to quicken plasma evolutions when parameters of the filled gas are held constant, and electron-ion heat conduction, radii and pressures are negative ones, when parameters of the incentive source are held constant. The experimental results in this paper provide support and reflection for the physical research on discharged capillary plasma and optimizing plasma channels in various applications.

Acknowledgements

This work was supported by the National Natural Science Foundation of China (Nos. 11975037, 61631001 and 11921006) and the National Grand Instrument Project (Nos. 2019YFF01014400 and 2019YFF01014404).

References

1. T. Tajima and J. M. Dawson, Phys. Rev. Lett. **43**, 267 (1979).
2. E. Esarey, P. Sprangle, J. Krall, and A. Ting, IEEE Trans. Plasma Sci. **24**, 252 (1996).
3. E. Esarey, C. B. Schroeder, and W. P. Leemans, Rev. Mod. Phys. **81**, 1229 (2009).
4. S. M. Hooker, Nat. Photonics **7**, 775 (2013).
5. X. Wang, R. Zgadzaj, N. Fazel, Z. Li, S. A. Yi, X. Zhang, W. Henderson, Y.-Y. Chang, R. Korzekwa, H.-E. Tsai, C.-H. Pai, H. Quevedo, G. Dyer, E. Gaul, M. Martinez, A. C. Bernstein, T. Borger, M. Spinks, M. Donovan, V. Khudik, G. Shvets, T. Ditmire, and M. C. Downer, Nat. Commun. **4**, 1988 (2013).
6. W. P. Leemans, B. Nagler, A. J. Gonsalves, Cs. Tóth, K. Nakamura, C. G. R. Geddes, E. Esarey, C. B. Schroeder, and S. M. Hooker, Nat. Phys. **2**, 696 (2006).
7. W. P. Leemans, A. J. Gonsalves, H.-S. Mao, K. Nakamura, C. Benedetti, C. B. Schroeder, Cs. Tóth, J. Daniels, D. E. Mittelberger, S. S. Bulanov, J.-L. Vay, C. G. R. Geddes, and E. Esarey, Phys. Rev. Lett. **113**, 245002 (2014).
8. A. J. Gonsalves, K. Nakamura, J. Daniels, C. Benedetti, C. Pieronek, T. C. H. de Raadt, S. Steinke, J. H. Bin, S. S. Bulanov, J. van Tilborg, C. G. R. Geddes, C. B. Schroeder, Cs. Tóth, E. Esarey, K. Swanson, L. Fan-Chiang, G. Bagdasarov, N. Bobrova, V. Gasilov, G. Korn, P. Sasorov, and W. P. Leemans, Phys. Rev. Lett. **122**, 084801 (2019).
9. R. Weingartner, S. Raith, A. Popp, S. Chou, J. Wenz, K. Khrennikov, M. Heigoldt, A. R. Maier, N. Kajumba, M. Fuchs, B. Zeitler, F. Krausz, S. Karsch, and F. Grüner, Phys. Rev. Spec. Top. Accel. Beams **15**, 111302 (2012).
10. G. R. Plateau, C. G. R. Geddes, D. B. Thorn, M. Chen, C. Benedetti, E. Esarey, A. J. Gonsalves, N. H. Matlis, K. Nakamura, C. B. Schroeder, S. Shiraishi, T. Sokollik, J. van Tilborg, Cs. Toth, S. Trotsenko, T. S. Kim, M. Battaglia,

https://doi.org/10.1017/hpl.2023.50 Published online by Cambridge University Press

Th. Stöhlker, and W. P. Leemans, Phys. Rev. Lett. **109**, 064802 (2012).
11. O. Lundh, J. Lim, C. Rechatin, L. Ammoura, A. Ben-Ismaïl, X. Davoine, G. Gallot, J.-P. Goddet, E. Lefebvre, V. Malka, and J. Faure, Nat. Phys. **7**, 219 (2011).
12. A. Buck, M. Nicolai, K. Schmid, C. M. S. Sears, A. Sävert, J. M. Mikhailova, F. Krausz, M. C. Kaluza, and L. Veisz, Nat. Phys. **7**, 543 (2011).
13. J. P. Couperus, R. Pausch, A. Köhler, O. Zarini, J. M. Krämer, M. Garten, A. Huebl, R. Gebhardt, U. Helbig, S. Bock, K. Zeil, A. Debus, M. Bussmann, U. Schramm, and A. Irman, Nat. Commun. **8**, 487 (2017).
14. C. G. R. Geddes, Cs. Toth, J. van Tilborg, E. Esarey, C. B. Schroeder, D. Bruhwiler, C. Nieter, J. Cary, and W. P. Leemans, Nature **431**, 538 (2004).
15. J. Faure, Y. Glinec, A. Pukhov, S. Kiselev, S. Gordienko, E. Lefebvre, J.-P. Rousseau, F. Burgy, and V. Malka, Nature **431**, 541 (2004).
16. S. P. D. Mangles, C. D. Murphy, Z. Najmudin, A. G. R. Thomas, J. L. Collier, A. E. Dangor, E. J. Divall, P. S. Foster, J. G. Gallacher, C. J. Hooker, D. A. Jaroszynski, A. J. Langley, W. B. Mori, P. A. Norreys, F. S. Tsung, R. Viskup, B. R. Walton, and K. Krushelnick, Nature **431**, 535 (2004).
17. A. Zigler, Y. Ehrlich, C. Cohen, J. Krall, and P. Sprangle, J. Opt. Soc. Am. B **13**, 68 (1996).
18. Y. Ehrlich, C. Cohen, A. Zigler, J. Krall, P. Sprangle, and E. Esarey, Phys. Rev. Lett. **77**, 4186 (1996).
19. Y. Ehrlich, C. Cohen, D. Kaganovich, A. Zigler, R. F. Hubbard, P. Sprangle, and E. Esarey, J. Opt. Soc. Am. B **15**, 2416 (1998).
20. D. Kaganovich, P. V. Sasorov, Y. Ehrlich, C. Cohen, and A. Zigler, Appl. Phys. Lett. **71**, 2925 (1997).
21. D. Kaganovich, A. Ting, C. I. Moore, A. Zigler, H. R. Burris, Y. Ehrlich, R. Hubbard, and P. Sprangle, Phys. Rev. E **59**, R4769 (1999).
22. R. F. Hubbard, Y. Ehrlich, D. Kaganovich, C. Cohen, C. I. Moore, P. Sprangle, A. Ting, and A. Zigler, AIP Conf. Proc. **472**, 394 (1999).
23. D. Kaganovich, P. Sasorov, C. Cohen, and A. Zigler, Appl. Phys. Lett. **75**, 772 (1999).
24. T. Hosokai, M. Kando, H. Dewa, H. Kotaki, S. Kondo, N. Hasegawa, K. Nakajima, and K. Horioka, Opt. Lett. **25**, 10 (2000).
25. E. Esarey, J. Krall, and P. Sprangle, Phys. Rev. Lett. **72**, 2887 (1994).
26. E. Esarey, P. Sprangle, J. Krall, and A. Ting, IEEE J. Quantum Electron. **33**, 1879 (1997).
27. A. J. Gonsalves, K. Nakamura, C. Lin, D. Panasenko, S. Shiraishi, T. Sokollik, C. Benedetti, C. B. Schroeder, C. G. R. Geddes, J. van Tilborg, J. Osterhoff, E. Esarey, C. Toth, and W. P. Leemans, Nat. Phys. **7**, 862 (2011).
28. M. Kirchen, S. Jalas, P. Messner, P. Winkler, T. Eichner, L. Hübner, T. Hülsenbusch, L. Jeppe, T. Parikh, M. Schnepp, and A. R. Maier, Phys. Rev. Lett. **126**, 174801 (2021).
29. N. H. Matlis, A. J. Gonsalves, S. Steinke, J. van Tilborg, B. Shaw, D. E. Mittelberger, C. G. R. Geddes, and W. P. Leemans, J. Appl. Phys. **119**, 074501 (2016).
30. L. Schaper, L. Goldberg, T. Kleinwächter, J.-P. Schwinkendorf, and J. Osterhoff, Nucl. Instrum. Methods Phys. Res. Sect. A **740**, 208 (2014).
31. N. H. Matlis, A. J. Gonsalves, S. Steinke, J. van Tilborg, E. H. Matlis, B. Shaw, D. E. Mittelberger, C. G. R. Geddes, and W. P. Leemans, J. Appl. Phys. **118**, 204506 (2015).
32. M. Fuchs, R. Weingartner, A. Popp, Z. Major, S. Becker, J. Osterhoff, I. Cortrie, B. Zeitler, R. Hörlein, G. D. Tsakiris, U. Schramm, T. P. Rowlands-Rees, S. M. Hooker, D. Habs, F. Krausz, S. Karsch, and F. Grüner, Nat. Phys. **5**, 826 (2009).
33. A. Butler, A. J. Gonsalves, C. M. McKenna, D. J. Spence, S. M. Hooker, S. Sebban, T. Mocek, I. Bettaibi, and B. Cros, Phys. Rev. Lett. **91**, 205001 (2003).
34. M. Chen, J. Luo, F.-Y. Li, F. Liu, Z.-M. Sheng, and J. Zhang, Light Sci. Appl. **5**, e16015 (2016).
35. E. A. Gibson, X. Zhang, T. Popmintchev, A. Paul, N. Wagner, A. Lytle, I. P. Christov, M. M. Murnane, and H. C. Kapteyn, IEEE J. Select. Top. Quantum Electron. **10**, 1339 (2004).
36. J. Luo, M. Chen, W. Y. Wu, S. M. Weng, Z. M. Sheng, C. B. Schroeder, D. A. Jaroszynski, E. Esarey, W. P. Leemans, W. B. Mori, and J. Zhang, Phys. Rev. Lett. **120**, 154801 (2018).
37. K. Nakajima, Light Sci. Appl. **7**, 21 (2018).
38. A. Zigler, M. Botton, Y. Ferber, G. Johansson, O. Pollak, E. Dekel, F. Filippi, M. P. Anania, F. Bisesto, R. Pompili, and M. Ferrario, Appl. Phys. Lett. **113**, 183505 (2018).
39. V. Shpakov, M. P. Anania, M. Bellaveglia, A. Biagioni, F. Bisesto, F. Cardelli, M. Cesarini, E. Chiadroni, A. Cianchi, G. Costa, M. Croia, A. Del Dotto, D. Di Giovenale, M. Diomede, M. Ferrario, F. Filippi, A. Giribono, V. Lollo, M. Marongiu, V. Martinelli, A. Mostacci, L. Piersanti, G. Di Pirro, R. Pompili, S. Romeo, J. Scifo, C. Vaccarezza, F. Villa, and A. Zigler, Phys. Rev. Lett. **122**, 114801 (2019).
40. R. D'Arcy, S. Wesch, A. Aschikhin, S. Bohlen, C. Behrens, M. J. Garland, L. Goldberg, P. Gonzalez, A. Knetsch, V. Libov, A. Martinez de la Ossa, M. Meisel, T. J. Mehrling, P. Niknejadi, K. Poder, J.-H. Röckemann, L. Schaper, B. Schmidt, S. Schröder, C. Palmer, J.-P. Schwinkendorf, B. Sheeran, M. J. V. Streeter, G. Tauscher, V. Wacker, and J. Osterhoff, Phys. Rev. Lett. **122**, 034801 (2019).
41. R. Pompili, D. Alesini, M. P. Anania, M. Behtouei, M. Bellaveglia, A. Biagioni, F. G. Bisesto, M. Cesarini, E. Chiadroni, A. Cianchi, G. Costa, M. Croia, A. Del Dotto, D. Di Giovenale, M. Diomede, F. Dipace, M. Ferrario, A. Giribono, V. Lollo, L. Magnisi, M. Marongiu, A. Mostacci, L. Piersanti, G. Di Pirro, S. Romeo, A. R. Rossi, J. Scifo, V. Shpakov, C. Vaccarezza, F. Villa, and A. Zigler, Nat. Phys. **17**, 499 (2021).
42. J. van Tilborg, S. Steinke, C. G. R. Geddes, N. H. Matlis, B. H. Shaw, A. J. Gonsalves, J. V. Huijts, K. Nakamura, J. Daniels, C. B. Schroeder, C. Benedetti, E. Esarey, S. S. Bulanov, N. A. Bobrova, P. V. Sasorov, and W. P. Leemans, Phys. Rev. Lett. **115**, 184802 (2015).
43. R. Pompili, M. P. Anania, M. Bellaveglia, A. Biagioni, S. Bini, F. Bisesto, E. Brentegani, G. Castorina, E. Chiadroni, A. Cianchi, M. Croia, D. Di Giovenale, M. Ferrario, F. Filippi, A. Giribono, V. Lollo, A. Marocchino, M. Marongiu, A. Mostacci, G. Di Pirro, S. Romeo, A. R. Rossi, J. Scifo, V. Shpakov, C. Vaccarezza, F. Villa, and A. Zigler, Appl. Phys. Lett. **110**, 104101 (2017).
44. J. van Tilborg, S. K. Barber, C. Benedetti, C. B. Schroeder, F. Isono, H.-E. Tsai, C. G. R. Geddes, and W. P. Leemans, Phys. Plasmas **25**, 056702 (2018).
45. C. A. Lindstrøm, E. Adli, G. Boyle, R. Corsini, A. E. Dyson, W. Farabolini, S. M. Hooker, M. Meisel, J. Osterhoff, J.-H. Röckemann, L. Schaper, and K. N. Sjobak, Phys. Rev. Lett. **121**, 194801 (2018).
46. R. Pompili, M. Anania, M. Bellaveglia, A. Biagioni, S. Bini, F. Bisesto, E. Brentegani, F. Cardelli, G. Castorina, E. Chiadroni, A. Cianchi, O. Coiro, G. Costa, M. Croia, D. Di Giovenale, M. Ferrario, F. Filippi, A. Giribono, V. Lollo, A. Marocchino, M. Marongiu, V. Martinelli, A. Mostacci, D. Pellegrini, L. Piersanti, G. Di Pirro, S. Romeo, A. Rossi, J. Scifo, V. Shpakov, A. Stella, C. Vaccarezza, F. Villa, and A. Zigler, Phys. Rev. Lett. **121**, 174801 (2018).

https://doi.org/10.1017/hpl.2023.50 Published online by Cambridge University Press

47. R. Pompili, G. Castorina, M. Ferrario, A. Marocchino, and A. Zigler, AIP Adv. **8**, 015326 (2018).
48. A. F. Pousa, A. Martinez de la Ossa, R. Brinkmann, and R. W. Assmann, Phys. Rev. Lett. **123**, 054801 (2019).
49. R. Pompili, E. Chiadroni, A. Cianchi, A. Del Dotto, L. Faillace, M. Ferrario, P. Iovine, and M. R. Masullo, Phys. Rev. Accel. Beams **22**, 121302 (2019).
50. S. K. Barber, J. H. Bin, A. J. Gonsalves, F. Isono, J. van Tilborg, S. Steinke, K. Nakamura, A. Zingale, N. A. Czapla, D. Schumacher, C. B. Schroeder, C. G. R. Geddes, W. P. Leemans, and E. Esarey, Appl. Phys. Lett. **116**, 234108 (2020).
51. T. Yang, H. Cheng, Y. Yan, M. Wu, D. Li, Y. Li, Y. Xia, C. Lin, and X. Yan, Phys. Rev. Accel. Beams **24**, 031301 (2021).
52. J. Bin, L. Obst-Huebl, J.-H. Mao, K. Nakamura, L. D. Geulig, H. Chang, Q. Ji, L. He, J. De Chant, Z. Kober, A. J. Gonsalves, S. Bulanov, S. E. Celniker, C. B. Schroeder, C. G. R. Geddes, E. Esarey, B. A. Simmons, T. Schenkel, E. A. Blakely, S. Steinke, and A. M. Snijders, Sci. Rep. **12**, 1484 (2022).
53. P. Sprangle and E. Esarey, Phys. Fluids B **4**, 2241 (1992).
54. P. Sprangle, E. Esarey, J. Krall, and G. Joyce, Phys. Rev. Lett. **69**, 2200 (1992).
55. P. Sprangle, B. Hafizi, and J. R. Peñano, Phys. Rev. E **61**, 4381 (2000).
56. P. Jha, N. Wadhwani, A. K. Upadhyaya, and G. Raj, Phys. Plasmas **11**, 3259 (2004).
57. E. Esarey, C. B. Schroeder, B. A. Shadwick, J. S. Wurtele, and W. P. Leemans, Phys. Rev. Lett. **84**, 3081 (2000).
58. C. Ren, B. J. Duda, R. G. Hemker, W. B. Mori, T. Katsouleas, T. M. Antonsen Jr., and P. Mora, Phys. Rev. E **63**, 026411 (2001).
59. P. Sprangle, J. R. Peñano, and B. Hafizi, Phys. Rev. E **66**, 046418 (2002).
60. A. K. Upadhyay, G. Raj, R. K. Mishra, A. Malviya, and P. Jha, Phys. Plasmas **14**, 093107 (2007).
61. A. K. Upadhyay, G. Raj, R. K. Mishra, and P. Jha, Phys. Plasmas **14**, 113105 (2007).
62. P. Sprangle, A. Ting, and C. M. Tang, Phys. Rev. Lett. **59**, 202 (1987).
63. P. Sprangle, A. Ting, and C. M. Tang, Phys. Rev. A **36**, 2773 (1987).
64. C. Benedetti, C. B. Schroeder, E. Esarey, and W. P. Leemans, Phys. Plasmas **19**, 053101 (2012).
65. E. Esarey and W. P. Leemans, Phys. Rev. E **59**, 1082 (1999).
66. L. Yu, H. M. Zhao, Q. Cao, X. Z. Zhu, J. L. Li, B. Y. Li, F. Liu, M. Chen, and Z. M. Sheng, Plasma Phys. Control. Fusion **64**, 075009 (2022).
67. N. A. Bobrova, A. A. Esaulov, J.-I. Sakai, P. V. Sasorov, D. J. Spence, A. Butler, S. M. Hooker, and S. V. Bulanov, Phys. Rev. E **65**, 016407 (2001).
68. B. H. P. Broks, K. Garloff, and J. J. A. M. van der Mullen, Phys. Rev. E **71**, 016401 (2005).
69. D. J. Spence and S. M. Hooker, Phys. Rev. E **63**, 015401 (2000).
70. D. M. Gaudiosi, B. Reagan, T. Popmintchev, M. Grisham, M. Berrill, O. Cohen, B. C. Walker, M. M. Murnane, H. C. Kapteyn, and J. J. Rocca, Phys. Rev. Lett. **96**, 203001 (2006).
71. D. J. Spence, P. D. S. Burnett, and S. M. Hooker, Opt. Lett. **24**, 993 (1999).
72. F. Brandi and L. A. Gizzi, High Power Laser Sci. Eng. **7**, e26 (2019).
73. A. J. Gonsalves, T. P. Rowlands-Rees, B. H. P. Broks, J. J. A. M. van der Mullen, and S. M. Hooker, Phys. Rev. Lett. **98**, 025002 (2007).
74. T. G. Jones, A. Ting, D. Kaganovich, C. I. Moore, and P. Sprangle, Phys. Plasmas **10**, 4504 (2003).
75. J. Kim, V. L. J. Phung, K. Roh, M. Kim, K. Kang, and H. Suk, Rev. Sci. Instrum. **92**, 023511 (2021).
76. Y. Ping, I. Geltner, A. Morozov, and S. Suckewer, Phys. Plasmas **9**, 4756 (2002).
77. H. S. Uhm, D. G. Jang, M. S. Kim, and H. Suk, Phys. Plasmas **19**, 024501 (2012).
78. G. Bagdasarov, P. Sasorov, A. Boldarev, O. Olkhovskaya, V. Gasilov, A. J. Gonsalves, S. Barber, S. S. Bulanov, C. B. Schroeder, J. van Tilborg, E. Esarey, W. P. Leemans, T. Levato, D. Margarone, G. Korn, and S. V. Bulanov, Phys. Plasmas **24**, 053111 (2017).
79. J. M. Garland, G. Tauscher, S. Bohlen, G. J. Boyle, R. D'Arcy, L. Goldberg, K. Põder, L. Schaper, B. Schmidt, and J. Osterhoff, Rev. Sci. Instrum. **92**, 013505 (2021).
80. A. Curcio, F. Bisesto, G. Costa, A. Biagioni, M. P. Anania, R. Pompili, M. Ferrario, and M. Petrarca, Phys. Rev. E **100**, 053202 (2019).
81. X.-Z. Zhu, B.-Y. Li, F. Liu, J.-L. Li, Z.-W. Bi, L. Lu, X.-H. Yuan, W.-C. Yan, M. Chen, L.-M. Chen, Z.-M. Sheng, and J. Zhang, Acta Phys. Sin. **71**, 095202 (2022).
82. A. Biagioni, M.P. Anania, M. Bellaveglia, E. Chiadroni, A. Cianchi, D. Di Giovenale, G. Di Pirro, M. Ferrario, F. Filippi, A. Mostacci, R. Pompili, V. Shpakov, C. Vaccarezza, F. Villa, and A. Zigler, J. Instrum. **11**, C08003 (2016).
83. P. S. Antsiferov, M. R. Akdim, and H. T. van Dam, Rev. Sci. Instrum. **78**, 123107 (2007).
84. J. Liu, W. Li, J. Liu, Z. Qin, W. Wang, R. Qi, Z. Zhang, C. Yu, M. Fang, K. Feng, Y. Wu, C. Wang, and R. Li, AIP Adv. **8**, 105204 (2018).
85. T. P. Rowlands-Rees, C. Kamperidis, S. Kneip, A. J. Gonsalves, S. P. D. Mangles, J. G. Gallacher, E. Brunetti, T. Ibbotson, C. D. Murphy, P. S. Foster, M. J. V. Streeter, F. Budde, P. A. Norreys, D. A. Jaroszynski, K. Krushelnick, Z. Najmudin, and S. M. Hooker, Phys. Rev. Lett. **100**, 105005 (2008).
86. T. G. Jones, K. Krushelnick, A. Ting, D. Kaganovich, C. I. Moore, and A. Morozov, Rev. Sci. Instrum. **73**, 2259–2265 (2002).
87. J. Daniels, J. van Tilborg, A. J. Gonsalves, C. B. Schroeder, C. Benedetti, E. Esarey, and W. P. Leemans, Phys. Plasmas **22**, 073112 (2015).
88. J. van Tilborg, A. J. Gonsalves, E. H. Esarey, C. B. Schroeder, and W. P. Leemans, Opt. Lett. **43**, 2776 (2018).
89. J. van Tilborg, A. J. Gonsalves, E. Esarey, C. B. Schroeder, and W. P. Leemans, Phys. Plasmas **26**, 023106 (2019).
90. A. J. Gonsalves, K. Nakamura, C. Lin, J. Osterhoff, S. Shiraishi, C. B. Schroeder, C. G. R. Geddes, Cs. Tóth, E. Esarey, and W. P. Leemans, Phys. Plasmas **17**, 056706 (2010).
91. M. Turner, A. J. Gonsalves, S. S. Bulanov, C. Benedetti, N. A. Bobrova, V. A. Gasilov, P. V. Sasorov, G. Korn, K. Nakamura, J. van Tilborg, C. G. Geddes, C. B. Schroeder, and E. Esarey, High Power Laser Sci. Eng. **9**, e17 (2021).
92. B. Broks, J. van Dijk, H. Bastiaens, K. Boller, and J. van der Mullen, J. Phys. D **39**, 2384 (2006).
93. V. V. Kotlyar and A. A. Kovalev, J. Opt. Soc. Am. A **27**, 372 (2010).
94. A. E. Siegman, *Lasers* (University Science Books, 1986).
95. A. D. Buckingham and C. Graham, Proc. R. Soc. Lond. Ser. A **337**, 275 (1974).
96. J. G. Zhu, M. J. Wu, Q. Liao, Y. X. Geng, K. Zhu, C. C. Li, X. H. Xu, D. Y. Li, Y. R. Shou, T. Yang, P. J. Wang, D. H. Wang, J. J. Wang, C. E. Chen, X. T. He, Y. Y. Zhao, W. J. Ma, H. Y. Lu, T. Tajima, C. Lin, and X. Q. Yan, Phys. Rev. Accel. Beams **22**, 061302 (2019).

https://doi.org/10.1017/hpl.2023.50 Published online by Cambridge University Press

97. R. Fletcher, *Practical Methods of Optimization: Unconstrained Optimization* (John Wiley & Sons, 1980).
98. X. Yuan, Y. Xu, R. Zhao, X. Hong, R. Lu, X. Feng, Y. Chen, J. Zou, C. Zhang, Y. Qin, and Y. Zhu, Optics **2**, 87 (2021).
99. M. J. Druyvesteyn and F. M. Penning, Rev. Mod. Phys. **12**, 87 (1940).
100. B. Mancinelli, L. Prevosto, J. C. Chamorro, F. O. Minotti, and H. Kelly, Plasma Chem. Plasma Process. **38**, 147 (2018).
101. T. D. Arber, K. Bennett, C. S. Brady, A. Lawrence-Douglas, M. G. Ramsay, N. J. Sircombe, P. Gillies, R. G. Evans, H. Schmitz, A. R. Bell, and C. P. Ridgers, Plasma Phys. Controll. Fusion **57**, 113001 (2015).

https://doi.org/10.1017/hpl.2023.50 Published online by Cambridge University Press